Journal of
Materials Chemistry B

PAPER

View Article Online
View Journal | View Issue

Cite this: J. Mater. Chem. B, 2018, 6, 1658

Biodegradable macroporous scaffold with nano-crystal surface microstructure for highly effective osteogenesis and vascularization

Linyang Chu,[a] Guoqiang Jiang,[b] Xi-Le Hu,[c] Tony D. James,[d] Xiao-Peng He,*[c] Yaping Li*[b] and Tingting Tang*[a]

Received 31st December 2017,
Accepted 3rd February 2018

DOI: 10.1039/c7tb03353b

rsc.li/materials-b

Using the hydrothermal calcination method, bovine cancellous bone was transformed into a degradable macroporous scaffold with a nano-crystal surface microstructure, capable of releasing bioactive ions. Compared with the control group, the presence of the nano-crystal microstructure of the material scaffold significantly promoted the gene expression of adhesion proteins including integrin and vinculin, thus facilitating attachment, spreading, proliferation and focal adhesion formation of MC3T3-E1 cells on the surface of the scaffold. Additionally, the release of active magnesium and calcium ions from the scaffold promoted expression of osteogenic genes and formation of calcium nodules in osteoblasts. Both *in vitro* and *in vivo* assays demonstrated that the three-dimensional interconnected porous architecture promoted vascularization and tissue integration. Our findings provide new insight into the development of degradable macroporous composite materials with "three-dimensional" surface microstructures as bone substitutes or tissue engineering scaffolds with potential for clinical applications.

1. Introduction

In the design and development of bone substitutes or tissue engineering scaffolds, it is important to take into account the complex composition and microstructure of mineralized human tissues.[1–3] An ideal material for bone repair or regeneration should be biocompatible, biodegradable, and bioactive for osteogenesis and vascularization. This requires the construction of well-interconnected three-dimensional structures and bioactive surfaces to facilitate the migration, adhesion and proliferation of bone cells.[4–7] In addition, bone substitutes or scaffolds should be degradable over time to provide space for bone and blood vessel growth.[8–11]

Hydroxyapatite (HA, $Ca_5(PO_4)_3(OH)$) and β-TCP ($Ca_3(PO_4)_2$) are widely used bone repairing materials in clinical medicine because of their recognized compatibility and osteoconductivity. However, HA is very stable in the body, which compromises the balance between bone growth and material degradation.[12] β-TCP is much more degradable than HA *in vivo*, but the unpredictable degradation rate and low mechanical stability limit its real application in bone regeneration.[13,14] To overcome these problems, multiphase bio-composite materials produced by a variety of techniques have been developed as bone substitutes with a well-balanced surface structure, pore size and connectivity, as well as degradation rate (Scheme 1).[15,16]

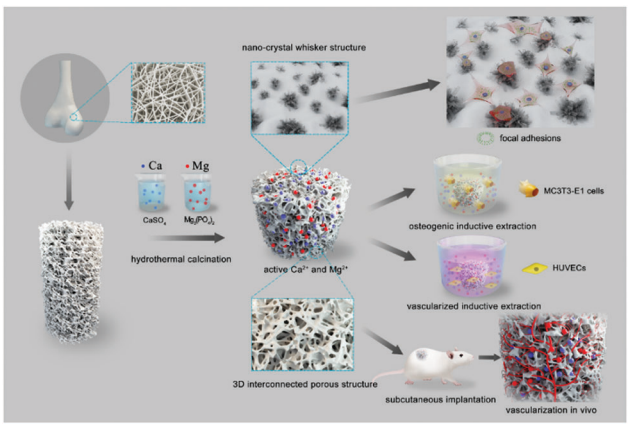

Scheme 1 Schematic illustration of the degradable macroporous scaffold with nano-crystal surface microstructure that is capable of releasing bioactive ions. Both *in vitro* and *in vivo* assays were used to evaluate the cytocompatibility, osteogenesis, vascularization and tissue integration of the scaffold.

[a] Shanghai Key Laboratory of Orthopedic Implants, Department of Orthopedic Surgery, Shanghai Ninth People's Hospital, Shanghai Jiao Tong University School of Medicine, Shanghai 200011, P. R. China. E-mail: ttt@sjtu.edu.cn
[b] Department of Orthopaedic Surgery, Affiliated Hospital of School of Medicine, Ningbo University, Ningbo 315211, P. R. China. E-mail: liyaping36@126.com
[c] Key Laboratory for Advanced Materials & Feringa Nobel Prize Scientist Joint Research Center, East China University of Science and Technology, Shanghai 200237, P. R. China. E-mail: xphe@ecust.edu.cn
[d] Department of Chemistry, University of Bath, Bath, BA2 7AY, UK

Herein, we have used the hydrothermal calcination method to achieve the conversion of bovine cancellous bone (HA as main ingredient) into degradable macroporous scaffold (HA/Ca/Mg). After hydrothermal reaction with the addition of Mg^{2+}, PO_4^{3-} and SO_4^{2-}, the composite material retained its original three-dimensional interconnected porous structure. More importantly, a nano-crystal, whisker microstructure was formed on the surface, which significantly improved the cell attachment and proliferation. Furthermore, the multiphase composite is degradable, capable of releasing bioactive Mg^{2+} and Ca^{2+} ions into the microenvironment. The Mg^{2+} and Ca^{2+} ions are essential elements in the human body and participate in many important metabolic activities.[17] It has been shown that Mg^{2+} and Ca^{2+} ions can effectively promote osteogenesis during bone repair.[18,19] Since a bone substitute or scaffold should also enable vascularization accelerating the formation of new bone, here, the vascularization of the developed material was also investigated systematically *in vitro* and *in vivo*. We believe that our composite material developed with a special, ''three-dimensional'' surface microstructure and the ability to release bioactive components will be a promising class of bone substitute and tissue engineering scaffold.

2. Experimental section

2.1 Materials

Bovine bone from femoral condylar cancellous bone was cut into raw bone pieces, which were then placed in an autoclave for heating for about 40–60 min at 115 °C. Then, the resulting material was cleaned using ultrasound 4–5 times. The treated raw bones were calcined at 800 °C for 6 h. After cooling, a macroporous scaffold was obtained. A solution containing Mg^{2+}, PO_4^{3-} and SO_4^{2-} was prepared with ion concentrations of 0.075 mol L^{-1}, 0.1 mol L^{-1} and 0.4 mol L^{-1}, respectively. The calcined bone and solution were mixed with a mass/volume rate of 100 mg mL^{-1} for hydrothermal reaction for 36 h at 75 °C. Then, the scaffold was taken out and dried at 100 °C for 24 h. Finally, the scaffold was placed in a temperature-controlled calcination furnace at 1050 °C (temperature rise rate was 2.5 °C min^{-1}) for 6 h to produce the desired macroporous HA/Ca/Mg composite. HA calcined bone without hydrothermal reaction and that hydrothermally reacted in Mg^{2+} and PO_4^{3-} solution (HA/Mg) were produced by the same protocol as controls. All specimens were sterilized by ethylene oxide for 3 h before cellular and animal tests.

2.2 Composition and surface characteristics

The composition of the scaffolds was analyzed using X-ray diffraction (XRD, Japan). The scaffolds were dried through an ethanol series, coated by gold sputtering, and examined using a scanning electron microscope (SEM, Japan) at an electron acceleration voltage of 1.5 kV in secondary electron detection mode. The element distribution of the scaffolds was determined using energy dispersive spectroscopy (EDS, Japan) at an electron acceleration voltage of 1.5 kV.

2.3 Microstructure measurement

The three-dimensional structure, porosity, pore connectivity and average pore size of the scaffolds were evaluated using a high-resolution micro-CT (μCT, Switzerland) at an isometric resolution of 25 μm; data were analyzed by procedures of micro-CT (RATOC, TRI/3D-bone).

2.4 Degradation test *in vitro*

The degradation test was carried out using previously reported methods.[20] Briefly, the scaffolds were immersed into 50 mM Tris–HCl solution at pH 7.40, 37 °C maintaining a weight-to-volume ratio of 0.2 g mL^{-1} with a shaking speed at 100 r min^{-1}. At different time points, the scaffolds were removed, cleaned with deionized water, and dried at 90 °C for 24 h. The scaffolds were re-immersed into fresh Tris–HCl solution under the same conditions. This process was repeated over a period of 4 weeks. The percentage of degradation was calculated by the following equation:

$$\text{Degradation (\%)} = 100 \times (W_0 - W_t)/W_0$$

where W_0 is the initial weight of the materials and W_t is the weight after treatment over time (t).

At each time point (6, 12, 24, 72 and 168 h), the scaffolds were taken out, and the concentrations of Mg^{2+}, Ca^{2+} and PO_4^{3-} in Tris–HCl solution were estimated using an inductively coupled plasma optical emission spectrometer (ICP-OES, USA). Meanwhile, the scaffolds were immersed into Dulbecco's Modified Eagle's Medium at the same weight-to-volume ratio and dissolution conditions mentioned above. At each time point, the pH values were measured using a flat membrane microelectrode (PB-10, Germany). All experiments were run in triplicate.

2.5 Evaluation of cytocompatibility *in vitro*

2.5.1 Cell spreading and focal adhesion formation. HA, HA/Mg, and HA/Ca/Mg scaffolds (column, 10 × 2 mm) were placed in 24-well plates. We chose the MC3T3-E1 cells,[21] a mouse preosteoblast line derived from mouse calvaria, since they have better stability in differentiation and cell phenotype, and less individual variation than human derived stem cells; these merits may lead to better reproducibility in experimentation. The cell suspension was seeded at a density of 3.0×10^4 cm^{-2} for each well. To assess cell spreading and focal adhesion formation after 6 h culturing, SEM and fluorescence staining were used. Briefly, cells were cultured on scaffolds for 6 h, fixed with 2.5% glutaraldehyde for 15 min, and then washed three times with PBS. Next, the samples for SEM analysis were treated in the same way as above. Meanwhile, for fluorescence staining, cells on scaffolds were fixed with 4% paraformaldehyde for 15 min, permeabilized with 0.1% Triton X-100 in PBS for 10 min and blocked with 5% albumin from bovine serum albumin (BSA). Then rabbit monoclonal antibody to vinculin (ab196454, Abcam) was used to stain the focal adhesions. Simultaneously, 4,6-diamidino-2-phenylindole (DAPI, Sigma) was used to stain the cell nuclei and rhodamine phalloidin (Molecular Probes, USA) was used to stain the filamentous actin of the cytoskeleton. At last, the samples

were observed by confocal laser scanning microscopy (CLSM, Germany).

To study the focal adhesion formation, intracellular integrin β1 and vinculin protein levels at 6 h were semi-quantitatively analyzed by western blotting. Collected proteins were separated using 8% SDS-PAGE gel, transferred onto PVDF membrane, and blocked with 5% skim milk solution for 1 h at room temperature. The samples were incubated with primary antibodies overnight and then incubated with an HRP-conjugated secondary antibody. Luminescence was detected and quantified by an imaging system (ChemiScope3600MINI, China). GAPDH was used as a loading control.

2.5.2 Cell attachment, viability and proliferation. As described above, the cells were co-cultured with the material in 24-well plates. The cell counting kit-8 (CCK-8) assay was used to analyze cell attachment at 6 and 12 h, and to analyze cell viability and proliferation at the time points of 1, 4 and 7 d. The modified OD values at 4 and 7 d were normalized to those at 1 d to calculate the proliferation rate of cells. In addition, fluorescence staining was used to observe cell viability on scaffolds at 1 d. DAPI and rhodamine phalloidin were used to stain the cell nuclei and cytoskeleton. Cells were imaged by CLSM.

2.6 Osteogenic differentiation *in vitro*

2.6.1 Cell culture and preparation of osteogenic inductive extraction. Extraction media of HA, HA/Mg, and HA/Ca/Mg scaffolds were prepared according to the International Organization for Standardization method (ISO 10993-12).[22] Briefly, the scaffolds were incubated in standard culture medium at a mass/volume ratio of 100 mg mL^{-1} at 37 °C. After 24 h, the supernatant was carefully collected and osteogenic inductive supplements were added, including 100 nM dexamethasone (Sigma), 50 μg mL^{-1} ascorbic acid (Sigma) and 10 mM β-glycerophosphate sodium (Sigma). Then, the osteogenic inductive extraction was filter sterilized and stored at 4 °C for further use. Afterwards, MC3T3-E1 cells were cultured with standard culture medium at a density of 5.0×10^4 cm^{-2} in 24-well plates for 24 h. Then, the medium was changed to osteogenic inductive extraction and refreshed every two days.

2.6.2 ALP, alizarin red staining and relative quantitative analysis. After 7, 14 and 21 d of culture, the ALP staining method was performed according to a previously reported procedure.[23] ALP activity was determined using an ALP microplate test kit (Beyotime, China) and observed directly by optical microscopy. The quantity of ALP in the cell lysates was measured at 520 nm using the Synergy HT microplate reader (Bio-Tek), then it was normalized to the corresponding total protein content determined by a BCA protein assay kit (ThermoFisher Scientific) according to the provided protocol. Meanwhile, calcium deposition (mineralization) was assessed by Alizarin Red S staining.[23] After culture for 21 and 28 d, cells were fixed in 4% paraformaldehyde for 15 min at 37 °C prior to being stained with 1% alizarin red solution (Sigma) for 45 min. Then, the samples were washed with PBS to remove the non-specific staining and observed directly by optical microscopy. For the quantitative analysis, 10% cetylpyridinium chloride (Sigma) in 10 mM sodium phosphate (Sigma) was added to the stained wells and then the mixed solutions were measured at 620 nm using the Synergy HT microplate reader (Bio-Tek).

Table 1 Primer sequences for real-time PCR

Target gene	Primers (5′-3′; F = forward; R = reverse)	Length
ALP	F: GGGCATTGTGACTACCACTCG	21
	R: CCTCTGGTGGCATCTCGTTAT	21
COL 1	F: AACAGTCGCTTCACCTACAGC	21
	R: GGTCTTGGTGGTTTTGTATTCG	22
OPN	F: CTTTCACTCCAATCGTCCCTAC	22
	R: CCTTAGACTCACCGCTCTTCAT	22
OCN	F: GGACCATCTTTCTGCTCACTCTG	23
	R: TTCACTACCTTATTGCCCTCCTG	23
GAPDH	F: AGGTCGGTGTGAACGGATTTG	21
	R: GGGGTCGTTGATGGCAACA	19

2.6.3 Expression of osteogenic related genes. The mRNA expression of several osteogenic differentiation-related genes, including osteocalcin (OCN), bone sialoprotein (BSP), collagen type I (COL1) and osteopontin (OPN), was quantitatively determined by real-time polymerase chain reaction (PCR).[21] The transcription levels of the genes were normalized to the housekeeping gene GAPDH. The sequences of the forward and reverse primers were demonstrated in Table 1. After 7, 14 and 21 days of culturing with the osteogenic inductive extraction, the TRIzol reagent (Ambion, USA) was used to collect total RNA according to the provided manufacturer's instructions. Then, reverse transcription was performed following the protocol of the Revert Aid first-strand cDNA synthesis kit (Fermentas, USA). Quantitative PCR (qPCR) was performed on an ABI 7500 machine (Applied Biosystems, USA) using the SYBR premix EX Taq PCR kit (Takara).

2.7 Bioactivity of vascularization *in vitro*

2.7.1 Cell culture and preparation of vascularized inductive extraction. Human umbilical vein endothelial cells (HUVECs) were purchased from the Shanghai Institutes for Biological Sciences and cultured in α-minimum medium supplemented with 10% fetal bovine serum and 1% penicillin/streptomycin. The extract medium of the scaffolds, as mentioned above, was supplemented with 1% ECGS (Endothelial Cell Growth Supplement, BD Biosciences). After that, the vascularized inductive extraction was filter sterilized and stored at 4 °C for use.

2.7.2 Capillary connections formation assay and quantitative analysis of VEGF. HUVECs were cultured in vascularized inductive extraction for 2 d. Then, Matrigel (BD Biosciences) was mixed with culture media at a ratio of 1 : 3 and added evenly to each well of a 96-well plate. HUVECs were separately resuspended and seeded on the gel at a density of 2×10^4 cells per well. After incubation for 4 h at 37 °C, the plate was observed by optical microscopy. At least 5 fields were digitally acquired for each substrate and the total number of capillary connections per field was counted by a blinded observer using the Image-Pro Plus software (Media Cybernetics, USA). Moreover, HUVECs were cultured in the vascularization inductive extraction for 12, 24 and 48 h. At each time point, the supernatant was collected and stored at −80 °C. The concentration of VEGF was determined by using a

Human Quantikine ELISA kit (R&D Systems, Canada) according to the manufacturer's instructions. Briefly, the supernatant was added to 96-well microplates that were coated with a monoclonal antibody to the factor of interest and incubated for 2 h. After washing with PBS, substrate solution was added and incubated for 30 min, and the reaction was terminated by addition of stop solution. VEGF levels were determined by measurement of the optical density at 450 nm using the Synergy HT microplate reader (Bio-Tek).

2.8 Tissue integration and vascularization analysis *in vivo*

2.8.1 Subcutaneous implantation of scaffolds in mice. A dorsum subcutaneous implantation model was established to evaluate vascularization of scaffolds *in vivo*.[24] All experimental procedures were approved and performed in accordance with the guidelines of the Animal Ethics Committee of Shanghai Ninth People's Hospital (The protocol registry number: A-2016-017). Briefly, 24 specific pathogen-free (SPF) 8-week-old male BALA/c mice were assigned randomly to three groups. The mice were initially anesthetized by using an intraperitoneal injection of 1% pentobarbital sodium (100 mg kg^{-1}) and the left dorsum was shaved and cleaned with 2% iodine prior to the procedure. Then, a deep subcutaneous pocket was made through an approximately 1.5 cm longitudinal skin incision over the left dorsum, in which one sample of a sterile scaffold was placed. The mice were housed in ventilated rooms and allowed to eat and drink after surgery. No antibiotics were administered, and no mortality occurred during the experiments.

2.8.2 Micro-CT based vascularization and histological analysis. Microfil perfusion (Microfil MV, USA) was conducted at 28 days after surgery. Briefly, after the pericardial cavity of the mice was exposed, the right auricle was snipped, then immediately heparinized saline (100 U mL^{-1}) was perfused into the apex of the heart at 2 mL min^{-1} using a syringe pump. A solution of Microfil prepared in a volume ratio of 4/5 of Microfil/diluent with 5% curing agent was perfused at a rate of 2 mL min^{-1} according to the manufacture's protocol.[24] Then, implanted scaffolds were harvested, fixed with 4% neutral-buffered formaldehyde for 48 h and decalcified with 9% formic acid for 4 weeks. The vascularization of scaffolds was reconstructed using micro-CT. Three-dimensional reconstruction of the newly formed vessels and their volume within scaffolds were analyzed by the software provided by the manufacturer. The evaluation was obtained from four animals randomly selected in each group.

After that, remaining scaffolds and surrounding soft tissues were retrieved 28 days after surgery. Then, they were immersed in 4% neutral-buffered formaldehyde for 48 h. The collected scaffolds and surrounding soft tissues were embedded into paraffin. The specimens were cut into sections parallel to the top surface of the scaffolds and prepared at a thickness of 5 μm (EXAKT-400, German). Hematoxylin eosin (H&E) and Masson's trichrome staining were used to assess the morphology and tissue integration. Furthermore, CD31 immunohistochemistry was used to assess vascularization. Sections were dewaxed in descending concentrations of alcohol and rehydrated. The slides were immersed in 3% hydrogen peroxide to block endogenous peroxidases and rinsed in PBS. They were immersed in 0.1% Triton-X100 in PBS for 15 min to allow penetration of the membrane. Antigen retrieval was carried out in a 10 mM warm citrate buffer for 15 min. Specific sites were saturated with normal goat serum for 40 min at 37 °C. Then, monoclonal anti-CD31 antibody (ab76533, Abcam) was used. The sections were incubated with biotinylated rabbit anti-rabbit immunoglobulins, washed in TBS for 5 min and incubated for 30 min with streptavidin–peroxidase (1 : 50, DAKO). The nuclei were counter stained with H&E for 2–3 seconds, washed in distilled water and finally covered with Aqua Tex (Merck, Germany). Four slides were then examined microscopically to take averages for statistical analysis.

2.9 Statistical analysis

All data are expressed as mean ± SD. Nonparametric test (Mann–Whitney U test), one-way analysis of variance (ANOVA) and the least significant difference (LSD) test were utilized to determine the level of significance; $p < 0.05$ was defined as statistically significant, and $p < 0.01$ was considered highly statistically significant. All statistical analyses of the data were performed using the SPSS software (v19.0, USA).

3. Results and discussion

3.1 Composition and microstructure characteristics

In this study, the hydrothermal calcination method has been used to convert bovine cancellous bone into a multiphase, degradable macroporous scaffold. The hydrothermal calcination process is necessary since it can remove immunogenic proteins and collagen, maintain the original three-dimensional interconnected porous structure and facilitate the formation of surface microstructure. The composition and microstructures of the different constructed scaffolds were first characterized by a diverse range of techniques. Fig. 1A shows the main composition of different scaffolds by XRD. The results showed that the HA scaffold was mainly composed of hydroxyapatite, in contrast, after calcination with hydrothermal reaction, $Ca_{(3-n)}Mg_n(PO_4)_2$ was produced in the HA/Mg scaffold. Moreover, in the HA/Ca/Mg scaffold, we observed that the content of $Ca_{(3-n)}Mg_n(PO_4)_2$ was relatively decreased along with the emergence of a $CaSO_4$ signal. The surface morphology of the three constructed scaffolds was characterized using SEM (Fig. 1B). The images showed that the HA/Mg scaffold had a rougher surface than the HA scaffold, which could be ascribed to the formation of $Ca_{(3-n)}Mg_n(PO_4)_2$ on the former surface. The elemental distributions of Ca, O, P, Mg, and S of different scaffolds obtained by EDS are shown in Fig. 2A. The images showed that Mg and S elements existed in the HA/Ca/Mg scaffold after hydrothermal reaction. A weaker Mg element signal was observed in the HA/Ca/Mg scaffold than the HA/Mg scaffold, which was consistent with the results of XRD analysis. Interestingly, after calcination, we observed the formation of a nano-crystal, whisker-like microstructure on the surface of the HA/Ca/Mg scaffold (Fig. 1B). Meanwhile, EDS

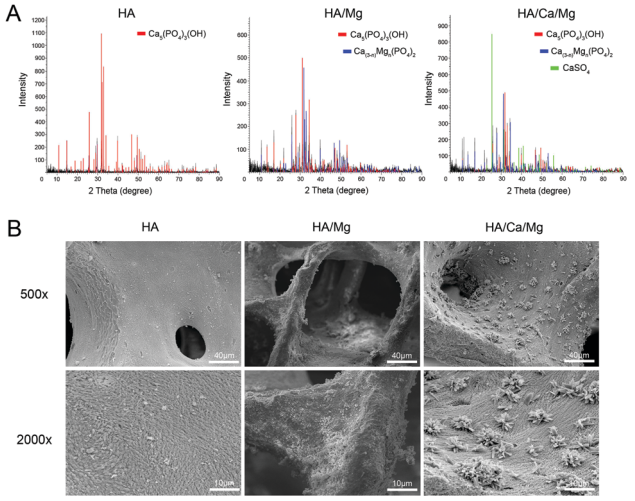

Fig. 1 Composition and surface characteristics of different scaffolds. (A) X-ray diffraction of scaffolds. (B) SEM images of the surface morphology of scaffolds.

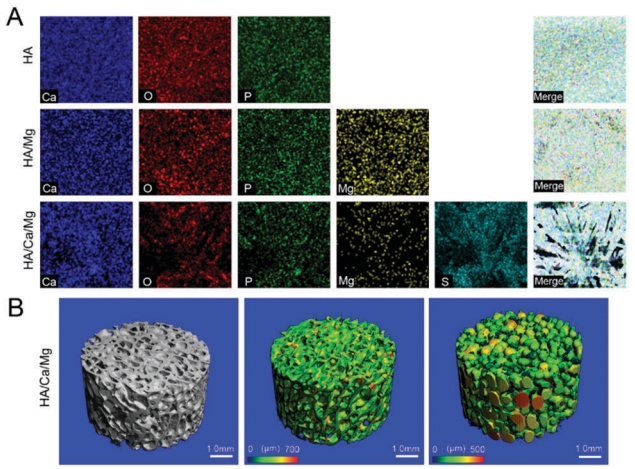

Fig. 2 Element distribution of scaffolds and 3D microstructure of HA/Ca/Mg scaffold. (A) Element distribution on the surface of various scaffolds. (B) 3D reconstructed images, porosity, pore connectivity and pore size of HA/Ca/Mg scaffolds obtained using micro-CT.

analysis of a nano-crystal whisker on the HA/Ca/Mg scaffold surface suggests that the composition consisted of sulfur element (Fig. 2A). The results of XRD and EDS analyses demonstrated that the main composition of the nano-crystal whisker structure was $CaSO_4$.

A bioactive scaffold should exhibit an ideal porosity with a homogeneous and interconnected porous structure, which is amenable for bone repair, vascular access and oxygen and tissue fluid exchange, providing physiologically active space for bone ingrowth.[25,26] The morphology and pore distribution of the HA/Ca/Mg scaffold were characterized using micro-CT (Fig. 2B). The scaffold possessed homogeneous and interconnected porous structures with a porosity of 82.4 ± 4.1%, connectivity of 100% and an average pore size of 370.3 ± 37.6 μm. There is no significant difference in the porous structures among all three groups.

3.2 Degradation test *in vitro*

Degradation rate is another important feature of bone substitutes and bone-tissue engineering scaffolds.[27] The ability of a scaffold to degrade within a reasonable timeframe can offer space for new bone formation and blood vessel growth. Whereas the degradation rate of HA is thought to be too slow for new bone growth, a too fast degradation rate would lead to unwanted bone defects in the implanted area.[12,13,28,29] The degradation of different scaffolds was measured in Tris–HCl solution. As shown in Fig. 3A, the weight loss of the HA/Ca/Mg scaffold after 4 weeks was about 21.8%, which is larger than that of the HA/Mg and HA group. The pH value of the HA/Mg scaffold increased rapidly within 0–24 h, and from 24 to 168 h, the pH continued to increase slightly. The HA/Ca/Mg scaffold had a relatively smaller pH fluctuation during 0 to 168 h. Due to limited degradation, the pH value of the HA scaffold hardly changed with time. Shown in Fig. 3C–E are the concentration changes of Mg^{2+}, Ca^{2+} and PO_4^{3-} released from the different scaffolds. The concentration of Mg^{2+}, Ca^{2+} and PO_4^{3-} in HA/Mg and HA/Ca/Mg increased rapidly from 0 to 72 h and began to stabilize from 72 to 168 h. In contrast, no significant changes in ion concentration of the HA scaffold were observed at different time points. Mg^{2+} plays a critical role in the body by mediating cell–extracellular matrix (ECM) interactions and controlling bone apatite structure and density.[30,31] The HA/Ca/Mg scaffold contains three different main ingredients and the dissolution rate between the various compositions was very different. Therefore, the scaffold could achieve gradient degradation, *i.e.* the material could be degraded rapidly in the early stage to release active Mg^{2+}, Ca^{2+} and PO_4^{3-}, followed by a stably sustained degradation to offer space for new bone formation.

3.3 Cell attachment, spreading, proliferation and focal adhesion formation on the scaffold surface

SEM was used to observe cell morphology on different scaffolds after 6 h. Fig. 4A shows less adhered cells on the HA and HA/Mg scaffolds than on the HA/Ca/Mg scaffold. In particular, on the

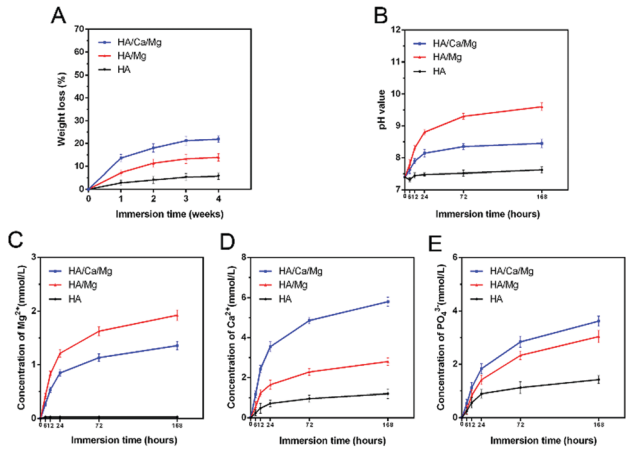

Fig. 3 Degradation test. (A) Weight loss rate of different scaffolds. (B) Changes in pH value. (C–E) Changes in concentration of Mg^{2+}, Ca^{2+} and PO_4^{3-}.

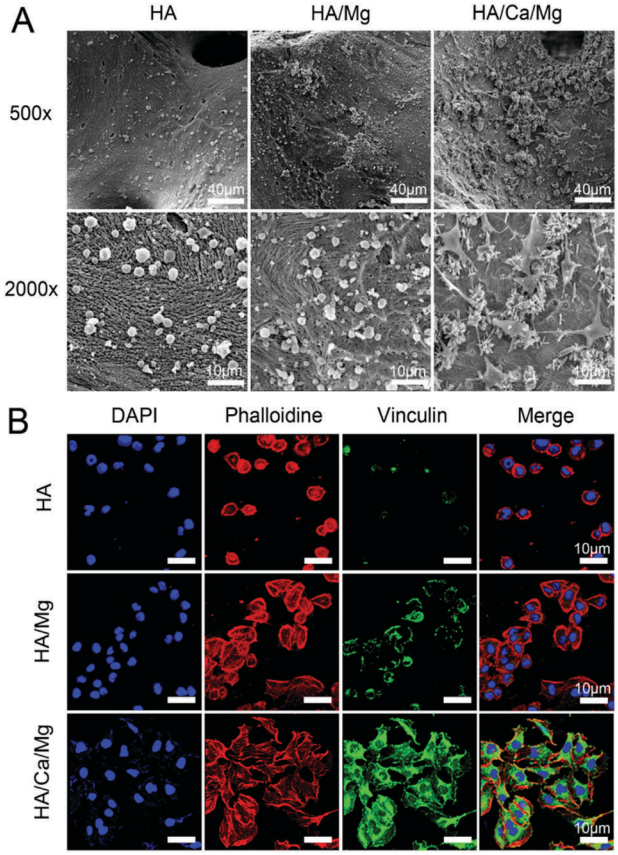

Fig. 4 Spreading and focal adhesion formation of MC3T3-E1 cells on the different scaffolds. (A) SEM images of cell morphology and spreading at 6 h on scaffolds. (B) The cytoskeletal morphology and focal adhesion formation of cells at 6 h on the scaffolds. Representative images of cells stained with DAPI for cell nuclei (blue), rhodamine phalloidin for actin filaments (red), and monoclonal antibody for focal adhesions (green). For CLSM, the scale bar for the row is shown in the merge image.

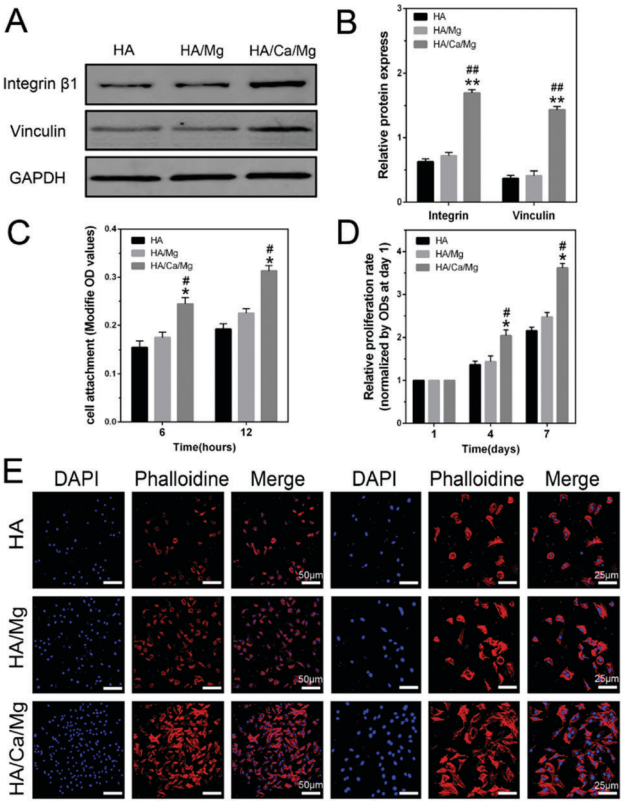

Fig. 5 Adhesion-related protein expression, attachment, viability and proliferation of MC3T3-E1 cells on the different scaffolds. (A and B) Western blotting for analysis of integrin β1 and vinculin in cells cultured for 6 h, and the results were quantified. (C) Cell attachment analysis at 6 and 12 h determined by CCK-8 assay. (D) Relative cell proliferation rates at 4 and 7 d determined by CCK-8 assay. (E) Cell viability evaluated by fluorescence staining at 1 d on scaffolds. DAPI for cell nuclei (blue) and phalloidin for actin filaments (red). $^{*}p < 0.05$ compared with HA scaffolds. $^{**}p < 0.01$ compared with HA scaffolds. $^{\#}p < 0.05$ compared with HA/Mg scaffolds. $^{\#\#}p < 0.01$ compared with HA/Mg scaffolds. The scale bar for the row is shown in the merge image.

HA/Ca/Mg scaffold, cells densely adhered to the nano-crystal whisker microstructure on which numerous filopodia pervaded. From the mechanism point of view, excellent cell spreading might be caused by an increased expression of adhesion related proteins including integrins and vinculin, thereby providing mechanical forces to the material surface.[32] Integrins are a family of transmembrane receptors that provide anchorage force for cellular adhesion by activating intracellular signalling pathways after ligand binding.[33] It has been proven that the expression of integrins is dependent on structure, roughness and wettability of a material surface.[32] Vinculin, on the other hand, a highly conserved actin-binding protein, is frequently used as a marker for focal adhesion.[34] Shown in Fig. 4B is the CLSM micrograph exhibiting cell spreading and focal adhesion formation on the different scaffolds. The cells grown on the HA/Ca/Mg scaffold displayed a clustered and confluent morphology with extensive actin filaments linking to adjacent cells. In contrast, cells on HA and HA/Mg scaffolds exhibited dispersed morphology with fewer actin filaments and a more reduced level of spreading. Meanwhile, the vinculin protein was immune-stained in the cytoplasm (visible as a green background inside the cells), suggesting the formation of abundant focal adhesions on HA/Ca/Mg. The intracellular protein expression of integrin β1 and vinculin after 6 h was further analyzed by western blotting (Fig. 5A and B). The results showed that integrin β1 and vinculin were detected at higher levels in cells grown on the HA/Ca/Mg scaffold ($p < 0.01$) than other scaffolds, which suggested that the microstructure of the HA/Ca/Mg scaffold could up-regulate expression of focal adhesion proteins in MC3T3-E1 cells, in agreement with the results of CLSM.

Cell attachment on scaffolds was evaluated by CCK-8 assay after 6 and 12 h. As shown in Fig. 5C, the counts of adherent cells on the HA/Ca/Mg scaffold were significantly higher than that on the HA and HA/Mg scaffolds at 6 and 12 h ($p < 0.05$). This result suggests that the HA/Ca/Mg scaffold could improve cell initial attachment on the material surface. We deduced that the initial cell attachment and spreading would affect cell proliferation on the material surface. This deduction was proven by the following analysis. The relative proliferation rate of cells on different scaffolds is shown in Fig. 5D. The cells on

the HA/Ca/Mg scaffold exhibited a higher proliferation rate than those on the HA and HA/Mg scaffolds at 4 and 7 d ($p < 0.05$). In addition, although the proliferation of cells on the HA/Mg scaffold was slightly higher than that on the HA scaffold, no significant differences were observed between the two scaffolds from day 1 to 7 d ($p > 0.05$). Moreover, CLSM was used to observe cell viability at 1 d. The cells stained with DAPI and phalloidine on the three scaffolds at 1 d are shown in Fig. 5E, which again corroborated the higher cell viability on the HA/Ca/Mg scaffold than other scaffolds. These results confirmed that the nano-crystal microstructure could promote cell attachment, spreading, proliferation and focal adhesion formation, thus improving the cytocompatibility of the scaffold. In our previous study,[35] we demonstrated that the topographical and morphological features of the nanostructured surface could regulate cell extension and cytoskeleton tension by the related signalling pathway of focal adhesions, which is similar to the results when using a HA/Ca/Mg scaffold. With this study, we envisioned that these biological effects might be related to the unique characteristics of the nano-crystal whisker-like structure, the nano-topological effect, and the enhanced adhesion protein adsorption level. Additional, relevant research will be carried out in the near future to confirm these theories. Moreover, we have already proven that the material's nano-surface could regulate osteogenic differentiation by affecting cell adhesion.[36] The cell adhesion mediated the activity of intracellular YAP/TAZ signalling by mechanotransduction, which could activate osteogenesis-related pathways and further promote the differentiation of cells. The focal adhesion formation plays a critical role in the transformation of physical characteristics into biological effects.

3.4 Osteogenic differentiation *in vitro*

The roles of bioactive Ca^{2+} and Mg^{2+} are beneficial for proliferation and differentiation of osteoblasts in the osteogenesis process.[8,17,37,38] Moreover, extracellular PO_4^{3-} can enter cells and subsequently the mitochondria, thereby promoting the synthesis of ATP. The ATP is then secreted, which can accelerate osteogenic differentiation of osteoblasts in bone regeneration by autocrine and/or paracrine signalling pathways.[39] ALP, Alizarin-red staining and relative quantitative analysis were carried out to better understand the influence of bioactive extraction of the scaffolds on the osteogenic differentiation of cells. Fig. 6A and B show the ALP and Alizarin-red intensity after 7, 14, 21 and 28 d of cell culturing. The intensity of the HA/Ca/Mg group was considerably stronger than that of the HA and HA/Mg groups. The relative ALP activity of the HA/Ca/Mg group was evidently higher than that of the HA group at all time points (Fig. 6C, $p < 0.01$). The results also indicated that the calcium nodule formation of the HA/Ca/Mg group was significantly higher than that of the HA and HA/Mg groups at 21 and 28 d (Fig. 6D, $p < 0.01$). Meanwhile, we examined the expression level of several critical osteogenic markers using quantitative real-time PCR assay at 7, 14 and 21 d (Fig. 7A–D). At 7 d, cells grown in osteogenic inductive extraction of the HA/Ca/Mg scaffold showed higher expression levels of ALP and COL1

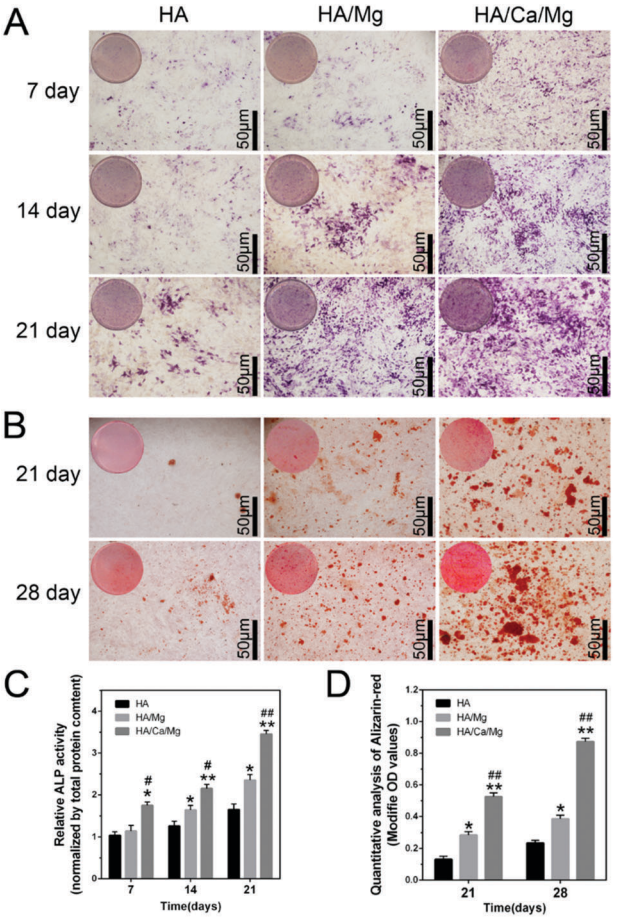

Fig. 6 Effects of osteogenic inductive extraction of scaffolds on osteogenesis of MC3T3-E1 cells. (A) ALP staining after 7, 14 and 21 d of cell culture in osteogenic inductive extraction. (B) Alizarin Red-S staining after 21 and 28 d of cell culture in osteogenic inductive extraction. (C and D) The quantitative analysis of ALP activity and alizarin Red-S staining. The ALP activity was normalized to the corresponding total protein content. *$p < 0.05$ compared with HA scaffolds. **$p < 0.01$ compared with HA scaffolds. $^{\#}p < 0.05$ compared with HA/Mg scaffolds. $^{\#\#}p < 0.01$ compared with HA/Mg scaffolds.

compared with other groups ($p < 0.05$). At 14 d, the gene expression of COL1 and OPN reached the peak in all three groups, and the ALP, COL1, OPN, and OCN mRNA levels of the HA/Ca/Mg group were significantly higher than those of the HA and HA/Mg groups ($p < 0.05$). Besides, at 21 d, the expression of four osteogenic mRNA of the HA/Ca/Mg group still maintained the highest level in all groups ($p < 0.05$). These results showed that osteogenic inductive extraction of HA/Ca/Mg scaffold could lead to a better osteogenesis ability than the other control scaffolds.

3.5 Bioactivity of vascularization *in vitro*

Vascularization is known to provide necessary oxygen and nourishment for cell repair, tissue ingrowth and bone reconstruction.[40] It was reported that vascularization could be dependent on the interaction between proteins and divalent ions (such as Ca^{2+} and Mg^{2+}) since the divalent ions may increase the affinity of some

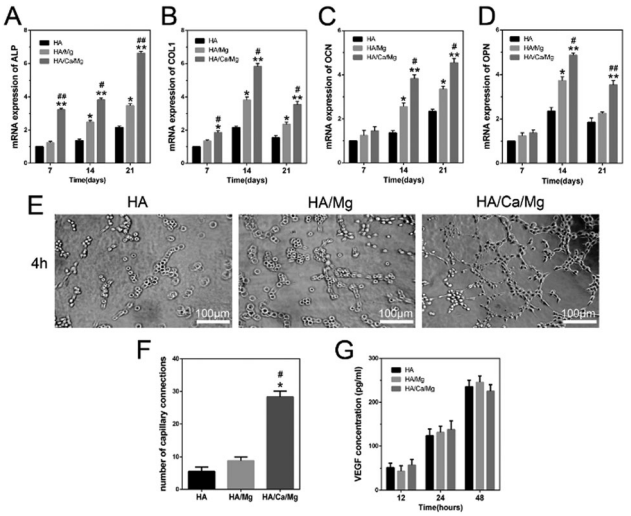

Fig. 7 Expression of osteogenic related genes of MC3T3-E1 cells and vascularization evaluation of HUVECs. (A–D) Relative mRNA expression of osteogenic differentiation related genes in cells grown with various osteogenic inductive extractions measured by real-time PCR after 7, 14 and 21 d. (E) Microscopy images of capillary connection formation on Matrigel for 4 h by HUVECs after culturing with different vascularized inductive extractions. (F) Total number of capillary connections formed per field by using Image-Pro Plus software. (G) The concentration of VEGF secreted by HUVECs cultured in vascularized inductive extraction for 12, 24 and 48 h. $^{*}p < 0.05$ compared with HA scaffolds. $^{**}p < 0.01$ compared with HA scaffolds. $^{\#}p < 0.05$ compared with HA/Mg scaffolds. $^{\#\#}p < 0.01$ compared with HA/Mg scaffolds.

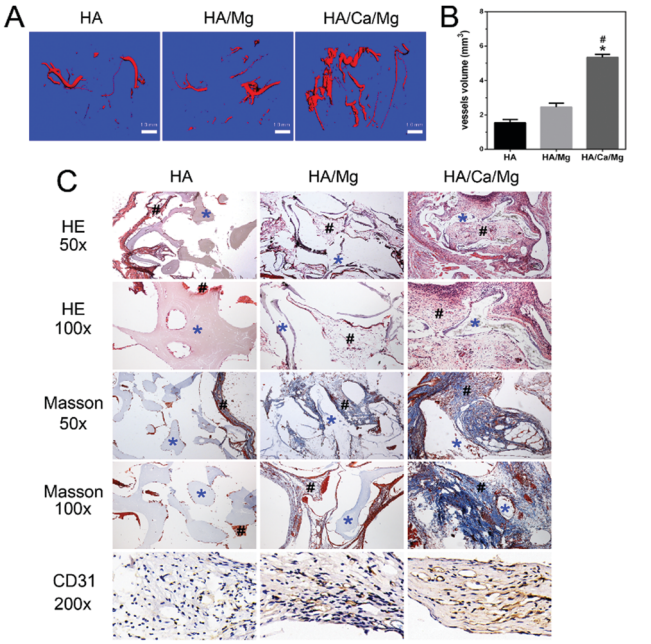

Fig. 8 Vascularization and tissue integration of various scaffolds *in vivo*. (A and B) Representative 3D images of micro-CT based newly formed vessels within scaffolds at 28 d after implantation and quantitative analysis of vessels volume. (C) Histological images of implanted scaffolds at 28 d after implantation. H&E and Masson's trichrome staining were used to assess the morphology and tissue integration. CD31 immunohistochemistry was used to assess vascularization (blue *, scaffold; black #, tissue). $^{*}p < 0.05$ compared with HA scaffolds. $^{\#}p < 0.05$ compared with HA/Mg scaffolds.

protein receptors in the vascularization process.[41] In this study, the capillary connection formation capability of HUVECs cultured with different vascularized inductive extractions was investigated by microscopy and quantified in terms of the number of capillary connections. Compared with the other two groups, HUVECs cultured with the extraction of HA/Ca/Mg scaffold after 4 h on Matrigel demonstrated a better capillary-like network formation ability (Fig. 7E). The number of capillary connections per field in the HA/Ca/Mg scaffold was significantly greater per field than other groups (Fig. 7F, $p < 0.05$). However, the ELISA results (Fig. 7G, $p > 0.05$) illustrated that the released divalent ions did not affect the amount of VEGF secreted by HUVECs, which is an important angiogenic growth factor in the vascularization process.[42,43] We hypothesized that divalent ions only increased the sensitivity of HUVECs to VEGF, but did not promote the secretion of VEGF during the vascularization process.

3.6 Tissue integration and micro-CT based analysis of vascularization *in vivo*

In tissue regeneration, vascularization can precede osteogenesis, and the enhanced neovascularization can accelerate new bone formation.[44,45] It has been demonstrated that angiogenesis is affected by the size of interconnected pore structure, which may lead to a faster vascularization and higher local oxygenation level.[26] Three-dimensional images of vascularization within the subcutaneously implanted scaffolds *in vivo* are shown in Fig. 8A, which indicate that more newly formed vessels were detected within the HA/Ca/Mg scaffold compared with the HA and HA/Mg scaffolds at 28 d after implantation. Meanwhile, the calculated volume of the newly formed vessels within the HA/Ca/Mg scaffold was significantly larger than that of the other two scaffolds (Fig. 8B, $p < 0.05$). Moreover, histological sections were stained with H&E and Masson's trichrome to assess the soft tissue integration *in vivo*. As demonstrated in Fig. 8C, the HA/Ca/Mg scaffold exhibited better tissue integration than HA and HA/Mg scaffolds, which indicated that the HA/Ca/Mg scaffold could offer a favourable micro-environment for tissue growth. Further, the results of CD31 immunohistochemistry showed a much better neovascularization of the HA/Ca/Mg scaffold than other scaffolds (Fig. 8C). These results showed that the HA/Ca/Mg scaffold displayed better biocompatibility *in vivo* after 28 days from implantation.

4. Conclusion

We used the hydrothermal calcination process to develop a bioactive scaffold with the original interconnected porous structure and novel nano-crystal whisker-like microstructures on the surface. Moreover, the scaffold can achieve gradient degradation with the capacity of releasing bioactive ions. Our results suggested that this scaffold with the nano-crystal surface effectively enhanced osteogenic cell attachment, spreading,

proliferation and focal adhesion formation. Notably, the scaffold promoted the osteogenic differentiation of pre-osteoblasts and capillary connection formation of HUVECs *in vitro* and demonstrated vascularization and tissue integration *in vivo*. We believe that these factors collectively have a synergistic effect on the biological processes. The unique scaffold developed herein might provide a new class of bioactive degradable composites as bone substitutes or tissue engineering scaffolds capable of osteogenesis and vascularization.

Conflicts of interest

There are no conflicts of interest to declare.

Acknowledgements

This research was financially supported by the National Key R&D Program (2016YFC1102100), Ningbo Municipal Natural Science Foundation (2010C500009) and Zhejiang Natural Science Foundation (2017LY17H060001). X.-P. He thanks the Natural Science Foundation of China (21722801 and 21572058) and the Shanghai Rising-Star Program (16QA1401400) (to X.-P. He) for generous financial support. The Catalysis And Sensing for our Environment (CASE) network is thanked for research exchange opportunities. T. D. J. wishes to thank the Royal Society for a Wolfson Research Merit Award and ECUST for a guest professorship.

References

1 H. Lu, T. Hoshiba, N. Kawazoe and G. Chen, *Biomaterials*, 2011, **32**, 2489–2499.
2 I. Zderic, P. Steinmetz, L. M. Benneker, C. Sprecher, O. Röhrle, M. Windolf, A. Boger and B. Gueorguiev, *J. Orthop. Transl.*, 2017, **8**, 40–48.
3 S. Bhumiratana, W. L. Grayson, A. Castaneda, D. N. Rockwood, E. S. Gil, D. L. Kaplan and G. Vunjak-Novakovic, *Biomaterials*, 2011, **32**, 2812–2820.
4 X. Liu, C. Bao, H. H. Xu, J. Pan, J. Hu, P. Wang and E. Luo, *Acta Biomater.*, 2016, **42**, 378–388.
5 A. Samadikuchaksaraei, M. Gholipourmalekabadi, E. Erfani Ezadyar, M. Azami, M. Mozafari, B. Johari, S. Kargozar, S. B. Jameie, A. Korourian and A. M. Seifalian, *J. Biomed. Mater. Res., Part A*, 2016, **104**, 2001–2010.
6 M. P. Lutolf, P. M. Gilbert and H. M. Blau, *Nature*, 2009, **462**, 433–441.
7 X. Zhang, H. A. Awad, R. J. O'Keefe, R. E. Guldberg and E. M. Schwarz, *Clin. Orthop. Relat. Res.*, 2008, **466**, 1777–1787.
8 I. Bajpai, D. Y. Kim, J. Kyong-Jin, I. H. Song and S. Kim, *J. Biomed. Mater. Res., Part B*, 2017, **105**, 72–80.
9 J.-S. Wang, M. Tägil, H. Isaksson, M. Boström and L. Lidgren, *J. Orthop. Transl.*, 2016, **6**, 10–17.
10 Y. Cai, J. Guo, C. Chen, C. Yao, S. M. Chung, J. Yao, I. S. Lee and X. Kong, *Mater. Sci. Eng., C*, 2017, **70**, 148–154.
11 C. Chai and K. W. Leong, *Mol. Ther.*, 2007, **15**, 467–480.
12 J. Brandt, S. Henning, G. Michler, W. Hein, A. Bernstein and M. Schulz, *J. Mater. Sci.: Mater. Med.*, 2010, **21**, 283–294.
13 L. Zheng, F. Yang, H. Shen, X. Hu, C. Mochizuki, M. Sato, S. Wang and Y. Zhang, *Biomaterials*, 2011, **32**, 7053–7059.
14 S. V. Dorozhkin, *Acta Biomater.*, 2010, **6**, 4457–4475.
15 X. Li, Y. Zhao, Y. Bing, Y. Li, N. Gan, Z. Guo, Z. Peng and Y. Zhu, *ACS Appl. Mater. Interfaces*, 2013, **5**, 5557–5562.
16 E. Culverwell, S. C. Wimbush and S. R. Hall, *Chem. Commun.*, 2008, 1055–1057.
17 D. Zhao, F. Witte, F. Lu, J. Wang, J. Li and L. Qin, *Biomaterials*, 2017, **112**, 287–302.
18 D. Zhao, S. Huang, F. Lu, B. Wang, L. Yang, L. Qin, K. Yang, Y. Li, W. Li, W. Wang, S. Tian, X. Zhang, W. Gao, Z. Wang, Y. Zhang, X. Xie, J. Wang and J. Li, *Biomaterials*, 2016, **81**, 84–92.
19 X. Chen, *J. Orthop. Transl.*, 2017, **10**, 1–4.
20 J. Wei, J. Jia, F. Wu, S. Wei, H. Zhou, H. Zhang, J. W. Shin and C. Liu, *Biomaterials*, 2010, **31**, 1260–1269.
21 R. Ma, S. Tang, H. Tan, J. Qian, W. Lin, Y. Wang, C. Liu, J. Wei and T. Tang, *ACS Appl. Mater. Interfaces*, 2014, **6**, 12214–12225.
22 C. Li, C. Jiang, Y. Deng, T. Li, N. Li, M. Peng and J. Wang, *Sci. Rep.*, 2017, **7**, 41331.
23 H. Tan, S. Guo, S. Yang, X. Xu and T. Tang, *Acta Biomater.*, 2012, **8**, 2166–2174.
24 Y. Yang, S. Yang, Y. Wang, Z. Yu, H. Ao, H. Zhang, L. Qin, O. Guillaume, D. Eglin, R. G. Richards and T. Tang, *Acta Biomater.*, 2016, **46**, 112–128.
25 T. M. Valverde, E. G. Castro, M. H. Cardoso, P. A. Martins-Junior, L. M. Souza, P. P. Silva, L. O. Ladeira and G. T. Kitten, *Life Sci.*, 2016, **162**, 115–124.
26 H. Kokemueller, S. Spalthoff, M. Nolff, F. Tavassol, H. Essig, C. Stuehmer, K. H. Bormann, M. Rucker and N. C. Gellrich, *Int. J. Oral Maxillofac. Surg.*, 2010, **39**, 379–387.
27 H. M. Wong, Y. Zhao, F. K. L. Leung, T. Xi, Z. Zhang, Y. Zheng, S. Wu, K. D. K. Luk, K. M. C. Cheung, P. K. Chu and K. W. K. Yeung, *Adv. Healthcare Mater.*, 2017, **6**, 1601269.
28 H. Zhao, W. Dong, Y. Zheng, A. Liu, J. Yao, C. Li, W. Tang, B. Chen, G. Wang and Z. Shi, *Biomaterials*, 2011, **32**, 5837–5846.
29 S. M. Best, A. E. Porter, E. S. Thian and J. Huang, *J. Eur. Ceram. Soc.*, 2008, **28**, 1319–1327.
30 Y. Zhang, J. Xu, Y. Ruan, M. Yu, M. O'Laughlin, H. Wise, D. Chen, L. Tian, D. Shi, J. Wang, S. Chen, J. Feng, D. Chow, X. Xie, L. Zheng, L. Huang, S. Huang, K. Leung, N. Lu, L. Zhao, H. Li, D. Zhao, X. Guo, K. Chan, F. Witte, H. Chan, Y. Zheng and L. Qin, *Nat. Med.*, 2016, **22**, 1160–1169.
31 H. S. Roh, C. M. Lee, Y. H. Hwang, M. S. Kook, S. W. Yang, D. Lee and B. H. Kim, *Mater. Sci. Eng., C*, 2017, **74**, 525–535.
32 N. Davidenko, C. F. Schuster, D. V. Bax, R. W. Farndale, S. Hamaia, S. M. Best and R. E. Cameron, *J. Mater. Sci.: Mater. Med.*, 2016, **27**, 148.
33 R. O. Hynes, *Cell*, 1992, **69**, 11–25.
34 T. Ohmori, Y. Kashiwakura, A. Ishiwata, S. Madoiwa, J. Mimuro, Y. Furukawa and Y. Sakata, *J. Biol. Chem.*, 2010, **285**, 31763–31773.
35 H. Pan, Y. Xie, K. Li, D. Hu, J. Zhao, X. Zheng and T. Tang, *RSC Adv.*, 2015, **5**, 101834–101842.

36 H. Pan, Y. Xie, Z. Zhang, K. Li, D. Hu, X. Zheng, Q. Fan and T. Tang, *Colloids Surf., B*, 2017, **152**, 344–353.
37 J. Zhang, X. Ma, D. Lin, H. Shi, Y. Yuan, W. Tang, H. Zhou, H. Guo, J. Qian and C. Liu, *Biomaterials*, 2015, **53**, 251–264.
38 B. Leitinger, A. McDowall, P. Stanley and N. Hogg, *Biochim. Biophys. Acta*, 2000, **1498**, 91–98.
39 Y. Shih, Y. Hwang, A. Phadke, H. Kang, N. Hwang, E. Caro, S. Nguyen, M. Siu, E. Theodorakis, N. Gianneschi, K. Vecchio, S. Chien, O. Lee and S. Varghese, *Proc. Natl. Acad. Sci. U. S. A.*, 2014, **111**, 990–995.
40 S. Ali, A. Singh, A. A. Mahdi and R. N. Srivastava, *J. Orthop. Transl.*, 2017, **10**, 5–11.
41 J. J. Grzesiak, G. E. Davis, D. Kirchhofer and M. D. Pierschbacher, *J. Cell Biol.*, 1992, **117**, 1109–1117.
42 J. He, M. L. Decaris and J. K. Leach, *Tissue Eng., Part A*, 2012, **18**, 1520–1528.
43 J. A. Maier, D. Bernardini, Y. Rayssiguier and A. Mazur, *Biochim. Biophys. Acta*, 2004, **1689**, 6–12.
44 S. H. Chen, M. Lei, X. H. Xie, L. Z. Zheng, D. Yao, X. L. Wang, W. Li, Z. Zhao, A. Kong, D. M. Xiao, D. P. Wang, X. H. Pan, Y. X. Wang and L. Qin, *Acta Biomater.*, 2013, **9**, 6711–6722.
45 W. Katagiri, T. Kawai, M. Osugi, Y. Sugimura-Wakayama, K. Sakaguchi, T. Kojima and T. Kobayashi, *Maxillofac. Plast. Reconstr. Surg.*, 2017, **39**, 8.